Effects of microstructure and local mechanical fields on intergranular stress corrosion cracking of a friction stir welded aluminum–copper–lithium 2050 nugget

Matthieu Dhondt [a,b], Isabelle Aubert [a], Nicolas Saintier [b,*], Jean Marc Olive [c]

[a] Université de Bordeaux, I2M, UMR 5295, 351 cours de la Libération, 33405 Talence Cedex, France
[b] Arts et Metiers ParisTech, I2M, UMR 5295, Esplanade des Arts et Métiers, 33405 Talence Cedex, France
[c] CNRS, I2M, UMR 5295, 351 cours de la Libération, 33405 Talence Cedex, France

A B S T R A C T

The effects of the microstructure and mechanical fields on intergranular stress corrosion cracking (IGSCC) of the nugget zone of heat treated welds obtained by friction stir welding in the AA2050 aluminum alloy have been investigated at different scales. At low strain rate, in 1.0 NaCl aqueous solution, IGSCC develops in the microstructure, whereas only pitting corrosion is observed without any mechanical stress. Based on surface observations, EBSD analysis and X-ray tomography, the key role of sub-millimetric textured bands (induced by the welding process) on the IGSCC is demonstrated. Analyses at a more local scale show the grain boundary (low angle boundary, special coincident site lattice boundary or high angle boundary) do not have a significant effect on crack initiation. Crystal plasticity finite element calculations show that the threshold normal stress at grain boundaries for IGSCC development is about 80% of the macroscopic stress. It is also highlighted by crystal plasticity calculations that there is a drastic effect of the local stress field on the shape of cracks. Finally, it is shown that plasticity induced residual stresses are sufficient for the formation of IGSCC.

Keywords:
A. Aluminum
A. Alloy
B. SEM
C. Stress corrosion
C. Intergranular corrosion
C. Welding

1. Introduction

Friction stir welding (FSW) is a solid state metal joining technique which is well suited for joining aluminum alloys such as the 2XXX and 7XXX alloys which show poor weldability by methods based on more traditional welding methods (arc welding for example). The difficulty in welding these materials is often attributed to the solidification process which causes a loss of alloying elements, the segregation process and porosity growth. The use of FSW technique and lightweight aluminum lithium alloys could significantly reduce the weight of aerospace structures by removing rivets, fasteners and overlapping areas. The FSW process generates strong microstructural changes due to high plastic deformation and frictional heat induced by the rotating tool. The joints consist of three zones involving specific microstructures, namely: heat affected zone (HAZ), thermo-mechanically affected zone (TMAZ) and weld nugget (WN) [1–4]. Previous work has shown that friction stir-welded joints in AA2050, AA2024, AA5456 and AA7050, exhibit more susceptibility to localized corrosion than the base metal [2,3,5,6]. For example, for the AA2024-T3 alloy without post-welding heat treatment, the HAZ is more sensitive to intergranular corrosion (IGC) than the base metal and has similar sensitivity to pitting corrosion [3]. For Al–Cu–Li alloys, the localized corrosion sensitivity depends on T1 (Al_2CuLi) precipitates, due to the potential difference between the precipitates and the matrix [7–10]. For pure aluminum and 2024 alloy, low angle boundaries (LAB) and special coincident site lattice (CSL) boundaries are usually more resistant to intergranular corrosion (IGC), compared to the random high angle boundaries (HAB) [11,12]. For the case of intergranular stress corrosion cracking (IGSCC), not only the grain boundary character distribution (GBCD) but also the mechanical fields play a key role. For the AA2024 alloy, internal stress [13], and external stress [14] cause an increase of the IGC growth rate. Some other mechanical parameters such as the stress intensity factor [15] or the strain rate [16–18] can modify the IGSCC degradation features. In addition, the temperature [15] or the current density [15,19,20] are known to affect the *SCC* behavior of aluminum alloys. As IGSCC is strongly correlated with the microstructure and in particular precipitates, it can be improved by post-weld heat treatments. Recently, it was highlighted that a

* Corresponding author. Tel.: +33 5 56 84 53 61; fax: +33 5 56 84 53 66.
E-mail address: nicolas.saintier@ensam.eu (N. Saintier).

post-welding heat-treatment improves the resistance to environmental degradation of 2050 FSW joints [2].

In this study, we focus on the nugget zone of AA2050 heat-treated welds, which is the most sensitive to IGSCC of the friction stir-welded joint. The effects of microstructure and mechanical fields on the IGSCC behavior have been investigated at different scales. At the macroscopic scale, the effect of external and internal stress on the degradation mode (pitting, cracks) was evaluated. At the mesoscopic scale, the role of the microstructure on the initiation and propagation of IGSCC was investigated. Finally, the role of the grain boundaries character was assessed at the microscopic scale.

2. Material and methods

The weld nugget used in this study was obtained by friction stir welding of two 15 mm thick sheets of AA2050-T3 (quenching and stretching), followed by a post-welding heat treatment at 155 °C during 30 h. EBSD maps performed along the gauge length of the specimens are shown in Fig. 1. They reveal a periodic crystallographic texture variation with a pattern of 500 µm, which corresponds to the FSW tool advance per revolution. This microstructure corresponds to the typical "onion rings" structure of FSW weld nuggets [21]. Despite heterogeneous texture, the nugget microstructure is relatively homogeneous in terms of grain size and shape, and consists of fine recrystallized equiaxed grains with an average grain diameter of 9 µm.

Stress corrosion cracking tests were performed on mechanically polished dumbbell shaped specimens machined in the middle of the nugget zone, the tensile direction corresponding to the welding direction L. The L–T plane is exposed to the corrosive environment (see Fig. 2). All specimens were mechanically polished up to 1/4 µm using OP-S solution before testing.

In order to highlight a possible internal and external stress effect on IGSCC, three types of tests were conducted:

1. Stress corrosion cracking tests (*SCC*) by the application of an external loading during immersion in 1.0 M NaCl.
2. Corrosion tests by immersion in 1.0 M NaCl of specimens previously pre-strained in air (*PRE*) to show the influence of residual stresses induced by the pre-straining.
3. Corrosion tests (*COR*) on tensile specimens by immersion of the heads of the specimen in 1.0 M NaCl.

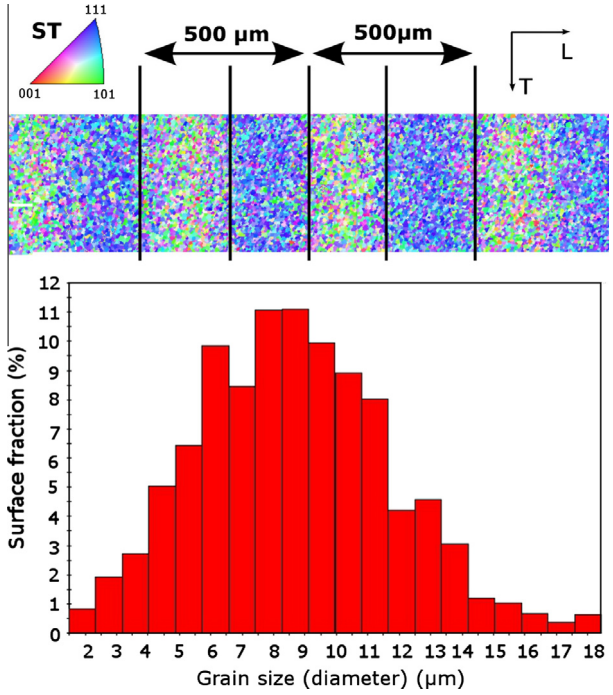

Fig. 1. EBSD map and grain size distribution of the weld nugget (step size of 2 µm).

All the specimens were left freely corroding. The immersion duration in NaCl was set to 1 h 30 for both (*PRE*) and (*COR*) tests. This time corresponds to the immersion time for stress corrosion cracks to develop during *SCC* tests conducted at a strain rate of $\dot{\epsilon} = 2 \cdot 10^{-6}\ s^{-1}$. A *SCC* cell was adapted to a 5 kN Deben Microtest tensile testing machine. The cell was designed so that only the gauge length of the sample is in contact with the corrosive solution. *SCC* tests were performed up to 1% plastic strain (1 h 30 of immersion). At that plastic strain level and immersion time well developed cracks were observed. For corrosion tests on pre-strained samples (*PRE*), a tensile test in air was performed at $\dot{\epsilon} = 5 \cdot 10^{-5}\ s^{-1}$ up to 10% plastic strain before immersion in the NaCl aqueous solution. The experimental conditions for each test are given in Table 1.

After the tests, the corrosion and stress corrosion induced damage were observed using an optical microscope OLYMPUS PMG3 and a scanning electron microscope (SEM) JEOL 840A. In addition, the microstructure surrounding cracked areas was identified by EBSD (EDAX high sensitivity camera) after polishing up to 1/4 µm using an OP-S solution. 3D crack morphologies were investigated by high resolution synchrotron X-ray tomography carried out at the European Synchrotron Radiation Facility (ESRF, ID19beamline).

The effect of intergranular stress field heterogeneities on the crack path was evaluated by means of finite element method that includes an explicit description of the microstructure surrounding stress corrosion cracks and crystal plasticity modeling. The 2D microstructure was first meshed according to grain morphologies and orientations obtained from EBSD analyses. 2D meshes were finally extruded to obtain a 3D model of the microstructure. Each generated aggregates contained approximately 300 grains and 512 grain boundaries (Fig. 6). The structural analyses were performed using the finite element (FE) code ZeBuLoN. The mechanical behavior of the material was described by a crystal plasticity elasto-plastic model as proposed by Cailletaud et al. [22].

Anisotropic elasticity was used to describe the elastic behavior. For the nugget microstructure, the cubic elasticity coefficients of pure aluminum were used (C_{1111} = 108 GPa, C_{1122} = 28.3 GPa, C_{1212} = 62 GPa). At the grain scale, inelastic deformation is mainly the result of plastic slip developing on the were orientated slip systems of the crystal. The resolved shear stress τ_s on each slip system s is given by Eq. (1).

$$\underline{\underline{m}}^s = \frac{1}{2}(\vec{n}^s \otimes \vec{l}^s + \vec{l}^s \otimes \vec{n}^s) \text{ and } \tau_s = \underline{\underline{\sigma}} : \underline{\underline{m}}^s \quad (1)$$

where $\vec{n}^s$ and $\vec{l}^s$ are the slip plane normal and the slip direction, respectively.

The plastic flow rate $\dot{\gamma}^s$ on the slip system s is given by Eq. (2) as follows:

$$\dot{\gamma}_s = \left\langle \frac{|\tau_s| - \tau_s^c}{K} \right\rangle^n \text{sign}(\tau_s) \quad (2)$$

where K and n characterize the material rate sensitivity, and τ_s^c the resolved shear stress threshold. Since in our case only monotonic loads are considered, the evolution of the critical resolved shear stress could be described by a nonlinear isotropic hardening law given in Eq. (3).

$$\tau_s^c = \tau_0^c + Q\sum_r h_{rs}(1 - e^{-bv_r}) \text{ with } v_r = \int_0^t |\dot{\gamma}^r| dt \quad (3)$$

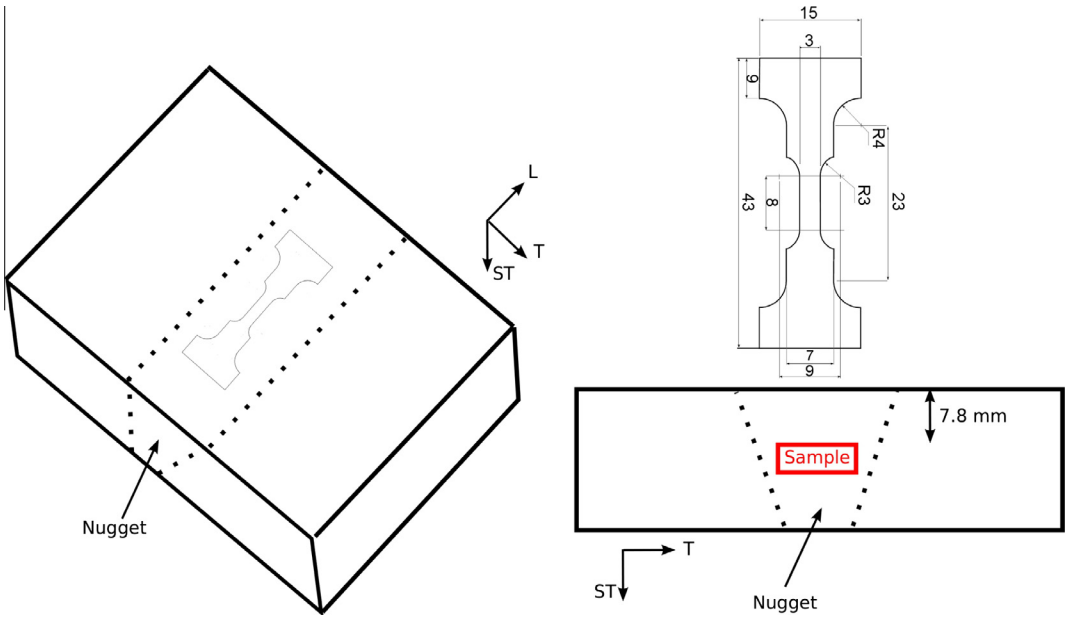

Fig. 2. Tensile samples machining.

Table 1
Experimental conditions.

Test	Solution	Immersion time	Tensile in air			Tensile in solution	
			$\dot{\epsilon}$ (s^{-1})	ϵ^{tot}_{max} (%)	Unloading	$\dot{\epsilon}$ (s^{-1})	ϵ^{tot}_{max} (%)
COR	NaCl 1 M	1 h 30	–	–	–	–	–
SCC	NaCl 1 M	1 h 30	$2{\cdot}10^{-6}$	0.5	No	$2{\cdot}10^{-6}$	1
PRE	NaCl 1 M	1 h 30	$5{\cdot}10^{-5}$	10	Yes	–	–

τ_0, Q and b were optimized by fitting the results obtained from the finite element calculations and the experimental tensile test curve. The obtained crystal plasticity model coefficients are: $K = 50$ MPa $s^{1/n}$, $n = 25$, $\tau_0^c = 66$ MPa, $Q = 50$ MPa, $b = 40$. Self hardening and latent hardening due to interactions between slip systems are introduced by the matrix h_{rs}. In this case, the interaction matrix was simplified by using Taylor hardening hypothesis i.e. $h_{rs} = 1$.

3. Results

3.1. Stress effect on IGSCC behavior

The typical degradation modes for each experimental condition (corrosion (*COR*), stress corrosion cracking (*SCC*) and corrosion with pre-strain (*PRE*)) are illustrated Fig. 3. For the corrosion tests, the weld nugget is slightly sensitive to pitting corrosion without any intergranular attack at an immersion time of 1H30 (see Fig. 3(a)). However, at longer time (3 days) and lower chloride concentration (0.7 M NaCl), both intragranular and intergranular corrosion were observed [23].

For the *SCC* tests, intergranular cracks were observed and no signs of transgranular transition could be found at that scale (see Fig. 3(b)). The main crack direction was systematically found to be perpendicular to the loading direction and limited crack branching was observed. After testing, crack length distribution and crack density were obtained from image analysis. The computed crack density is around 170 cracks per mm^2 and the crack length distribution is shown in Fig. 4. The average crack length is 20 µm. However, the length of more than 50% of the cracks is lower than 10 µm. The length of a slight fraction of them (∼2%) is higher than 100 µm. The longest cracks were found to appear fairly periodically at the surface as shown in Fig. 5, with a characteristic length of 500 µm along the tensile direction. Further analysis of this periodicity will be proposed in the next section.

For corrosion tests on pre-strained samples, IGSCC develops without any preferential propagation directions as shown in Fig. 3(c). In this case the driving mechanical force is the residual stress field induced by pre-straining at the microstructural scale (intergranular strain incompatibilities). To understand the

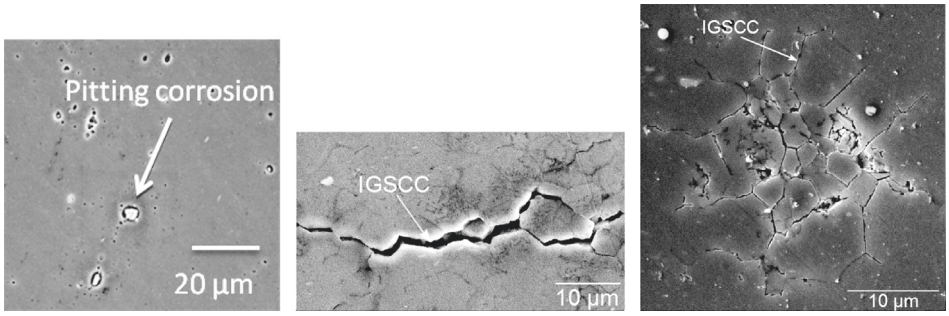

(a) *COR* (b) *SCC* (c) *PRE*

Fig. 3. SEM images taken after (a) a corrosion test, (b) a *SCC* test, and (c) a corrosion test on a pre-strained sample.

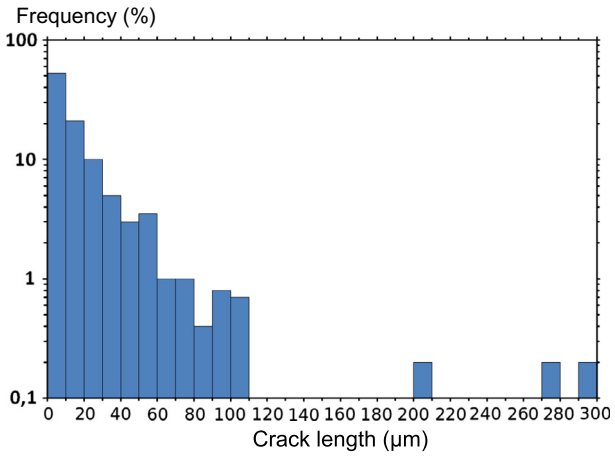

Fig. 4. Crack length distribution after *SCC* test.

difference in term of crack morphology between the *SCC* and *PRE* tests, finite element (FE) calculations were performed. Two uniaxial loading conditions were simulated: a tensile test along the longitudinal direction up to 10% strain, and a tensile test (L direction) up to 10% strain followed by unloading to zero macroscopic stress, simulating the *SCC* test and the *PRE* test, respectively. The FE calculations provided the local stress field and eigen vectors defining the principal stress directions. For each grain boundary and each loading condition, the projections in L–T, L–ST and T–ST planes of the unit eigen vectors for the highest principal stress are shown in Fig. 7. For the *SCC* test, the eigen vectors are mainly oriented in the L direction (i.e. the tensile direction, see Fig. 7(b)). In the case of the *PRE* test, the average stress over the polycrystal is zero, but at the local scale, a residual stress field is generated by the pre-straining. It can be seen from Fig. 7(c), that the associated distribution of the eigen vector directions related to the highest principal stress is uniform in the different planes, i.e. there is no preferential direction. For both loading conditions the experimentally observed intergranular cracks orientations distributions correlate well the calculated maximum eigen stress orientation distributions.

3.2. Effect of the microstructure on IGSCC at the mesoscopic scale

To obtain information on the role of the microstructure on IGSCC at the mesoscopic scale, EBSD analyses were performed on

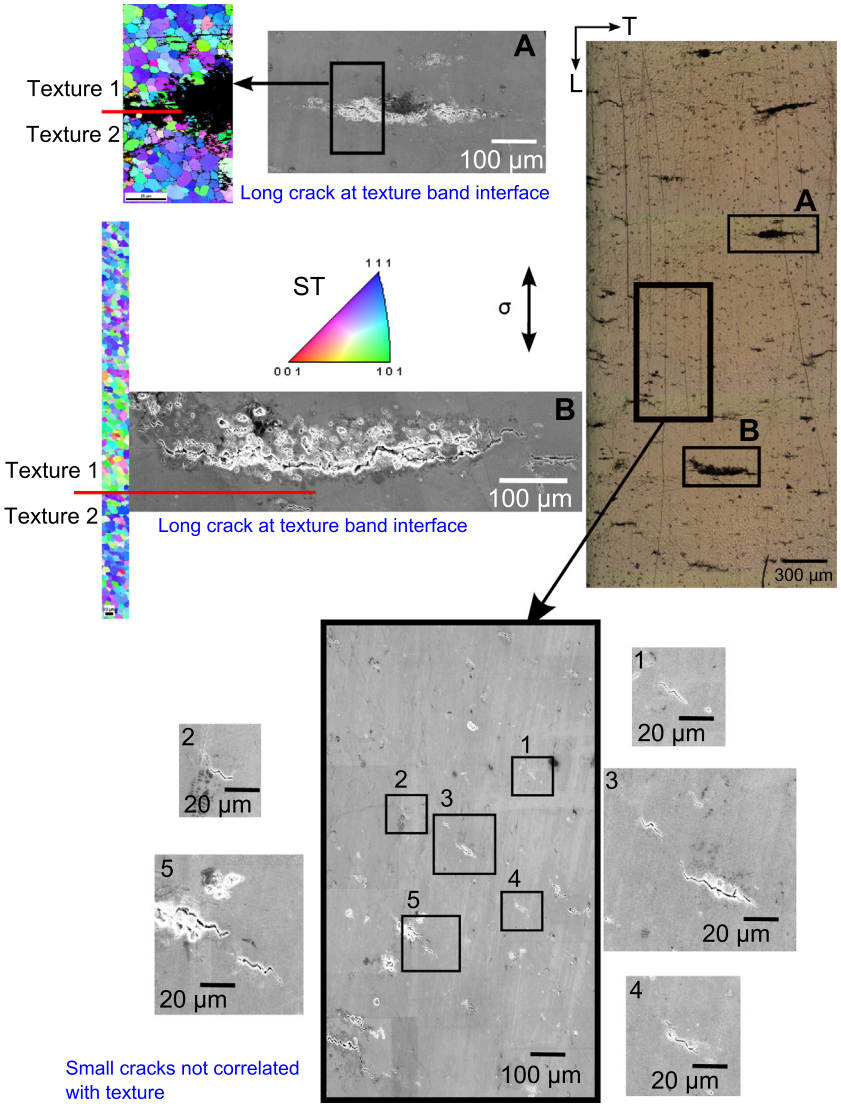

Fig. 5. Relation between cracks and microstructure at mesoscopic scale. Optical image of the sample submitted to *SCC* test at $\dot{\epsilon} = 2 \cdot 10^{-6}\ s^{-1}$ strain rate in NaCl 1 M, SEM images of details and EBSD maps performed in the vicinity of the longest cracks.

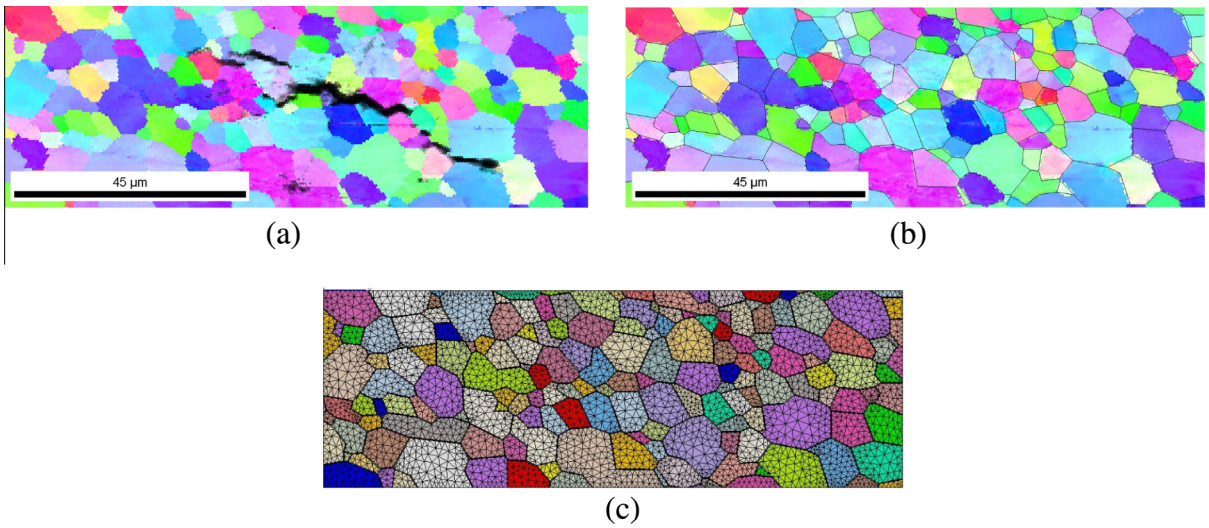

Fig. 6. Finite-element mesh generation from an EBSD map performed around an intergranular stress corrosion crack: (a) EBSD map performed around an intergranular stress corrosion crack, (b) EBSD map after cleaning by grain dilatation, and (c) 2D mesh.

the specimens after *SCC* tests. Optical and SEM images of the specimen as well as crystallographic orientation maps of selected zones are shown in Fig. 5. Two main comments can be made based on these observations. Firstly, the spatial distribution of the longest cracks along the gauge length has a periodicity consistent with the microstructural characteristic length of about 500 µm described in Section 2. Secondly, The EBSD maps of the zones containing cracks clearly show that the longest cracks initiate and propagate along the interface between the two different texture sets. Long focal video optical microscopy used *in situ* during *SCC* tests confirmed that the longest cracks initiate early in the test and occur at the interface between textured bands. The detrimental effect of these texture variations can be related to stress–strain field localization induced by the change of texture. A dedicated study on this aspect will be published in a forthcoming paper. Small cracks are fairly homogeneously distributed on the specimen surface (three examples of them are shown in Fig. 5). Small cracks initiate later in the test corresponding to higher macroscopic stress/strain. The initiation criterion of IGSCC is discussed in the following sections.

EBSD analyses provide 2D information concerning the microstructure and crack features. X-ray microtomography analyses were then performed to determine the 3D IGSCC cracks morphologies. A volume of $2.8 \times 1.4 \times 1\ \text{mm}^3$ in the gauge length was scanned with a voxel size of 0.35 µm allowing the detection of all cracks observed on the optical image. From the X-ray tomography image (see Fig. 8) it can clearly be observed that the longest cracks, initiated at a texture band interface, are also the deepest. The propagation of these long cracks occurs in the L–ST plane, along the texture band boundary which is oriented to 45° with respect to the tensile direction as shown in Fig. 8(c). This result confirms the key role of crystallographic orientations on IGSCC cracks propagation. In the next section, the effect of local microstructural parameters on the IGSCC is investigated.

3.3. Effect of grain boundary characteristics on IGSCC

Three grain boundary types can be distinguished: low angle boundaries (LAB) up to 15° misorientation, special coincident site lattice (CSL) and non-CSL random high angle boundaries (HAB). The crystallographic character of grain boundaries was identified from EBSD maps taken in the vicinity of IGSCC cracks as shown Fig. 9. A statistical analysis was performed from EBSD maps on 18 zones containing cracks, to highlight the effect of local grain orientations on the IGSCC. The following local parameters were investigated:

1. Grain boundary character distribution (GBCD): LAB, CSL boundaries and HAB.
2. Grain boundary geometric orientation (GBGO) characterized by the angle θ relative to the tensile direction as shown in Fig. 9.

In order to differentiate grain boundaries associated with the crack initiation process from those involved in crack propagation, only small cracks were considered (typical crack length to grain size ratio of 10–15) and a symmetric propagation of cracks was assumed. Due to the damage induced by corrosion in the vicinity of the longest crack mouth as seen in Fig. 5, it was not possible to make the same analysis as for small cracks. Small cracks represent 95% of the total cracks in the sample as seen in Fig. 4, ensuring the representativeness of the analysis. Under these assumptions, the grain boundaries located at the center of the cracks were considered to be related to the initiation stage (typically one to three depending on the local configuration, such grain boundaries will be noted IGI in the following), while the others relate to the propagation process (IGP grain boundaries). To compare cracked and uncracked grain boundaries, the crystallographic character of grain boundaries was analyzed in uncracked zones. The statistical analysis shown in Fig. 10 was performed using 56 IGI, 192 IGP and 1200 uncracked GB. Whatever the type of grain boundaries (uncracked, IGI, or IGP), the grain boundary distributions are quite similar and HAB is the most prevalent crystallographic character. The proportion of uncracked LAB is slightly higher than the cracked ones. In addition IGI and IGP have got a slightly higher proportion of CSL boundaries than noncracked ones. However, for both cases, LAB and CSL deviations are not significant enough to conclude any particular sensitivity of the intergranular stress corrosion cracking initiation and propagation on the crystallographic character of the grain boundary.

EBSD maps were analyzed to highlight a possible effect of the grain boundary geometric orientation (GBGO) on IGSCC propagation. The aim is to evaluate possible local crack orientation deviation from the observed macroscopic crack orientation (i.e. perpendicular to the applied macroscopic stress). Fig. 11 shows the relative cumulative frequency of the GB angle, θ, for cracked and uncracked GB's (θ is defined Fig. 9). For each value of θ, this

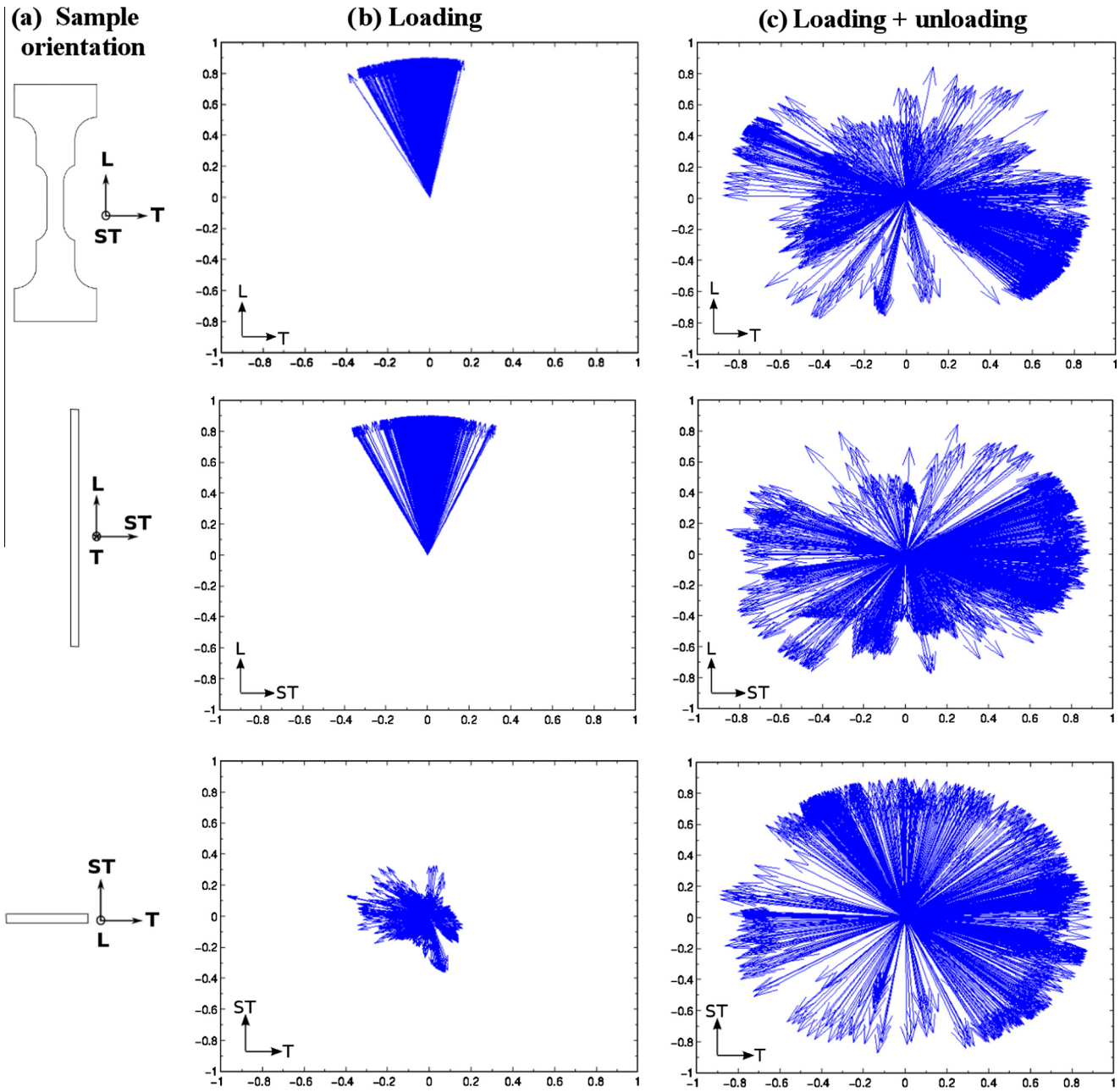

Fig. 7. Visualization of the direction of the highest principal stress in planes L–T, L–ST and T–ST: (a) Details of the sample orientation. (b) and (c) Projection, for each grain boundary, of the normalized eigen vectors associated to the highest principal stress in plane L–T, L–ST and T–ST corresponding to the loading and the loading–unloading simulation, respectively.

figure gives the relative cumulative frequency of GB having a GB angle equal or lower than θ. For cracked boundaries, the grain boundaries corresponding to the location of crack initiation are also highlighted. For uncracked grain boundaries, the observed cumulative frequency is characteristic of a uniform distribution that corresponds to the equiaxed nature of the microstructure (grain shape). More than 50% of the cracked grain boundaries are oriented at an angle higher than 70° while it represents only 20% of the total grain boundary population. It is noticeable that grain boundaries at crack initiation are not systematically found at the highest angles but are well spread in the 50–90° range. Due to elastic anisotropy, it is not possible to directly associate a GBGO to a normal stress. For this reason the normal stress to the grain boundaries was obtained from FE computation. The corresponding relative cumulative frequency function is given in Fig. 12. While uncracked grain boundaries experience normal stresses ranging from −300 to 400 MPa, cracked GB experience only positive normal stresses. 90% of cracked grain boundaries experience normal stresses above 200 MPa while it represents only 55% of uncracked GB. The analyses of GB at crack initiation shows that there exists a normal stress threshold of about 200 MPa in order to initiate corrosion cracking.

4. Conclusions

The effects of the microstructure and mechanical loading on the intergranular stress corrosion cracking of a friction stir welded nugget on the AA2050 aluminum alloy were investigated at different scales in 1.0 M NaCl aerated solution at room temperature.

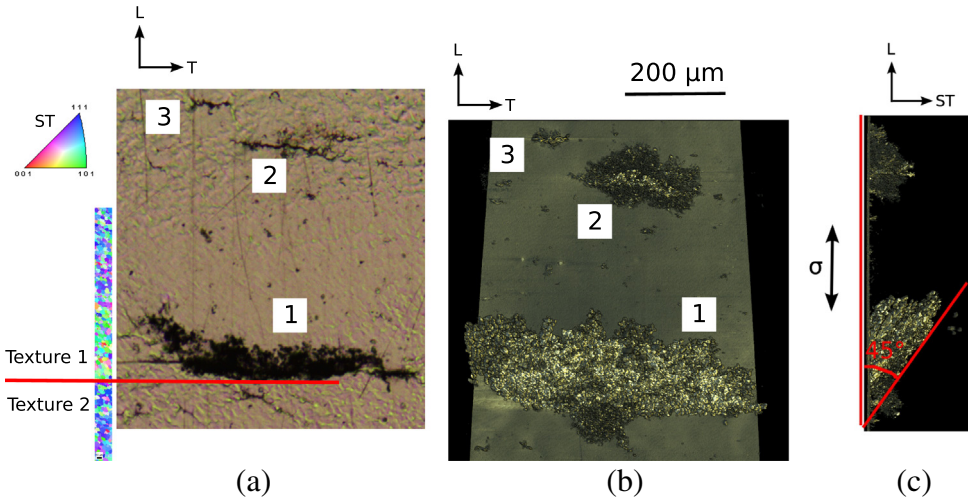

Fig. 8. Crack 3D morphology after *SCC* test at $\dot{\epsilon} = 2 \cdot 10^{-6}\ s^{-1}$ strain rate in NaCl 1 M. (a) Optical image and corresponding EBSD map, (b) X-ray tomography scan in L–T plane, and (c) X-ray tomography scan in L–ST plane.

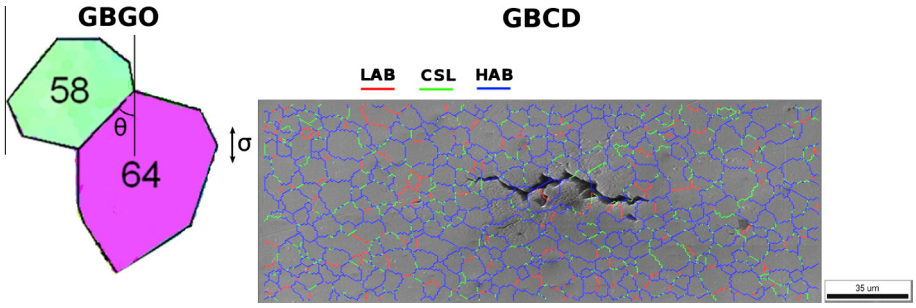

Fig. 9. Definition of grain boundary geometric orientation (GBGO) and grain boundary character distribution (GBCD).

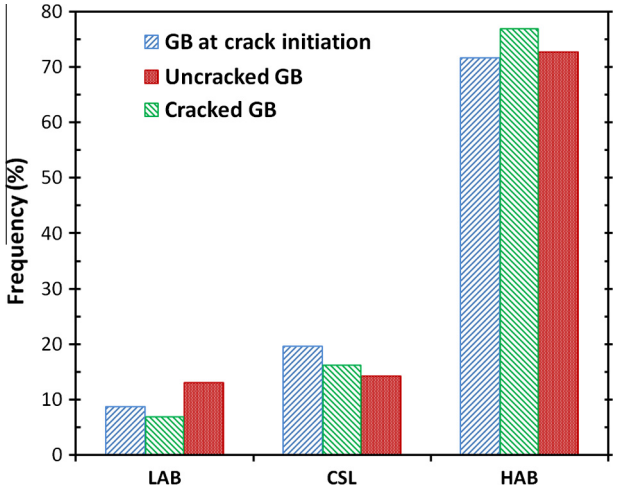

Fig. 10. Grain boundary distribution for each crystallographic character. The analysis was performed on 56 grain boundaries at crack initiation, 192 cracked grain boundaries and 1200 uncracked grain boundaries, respectively.

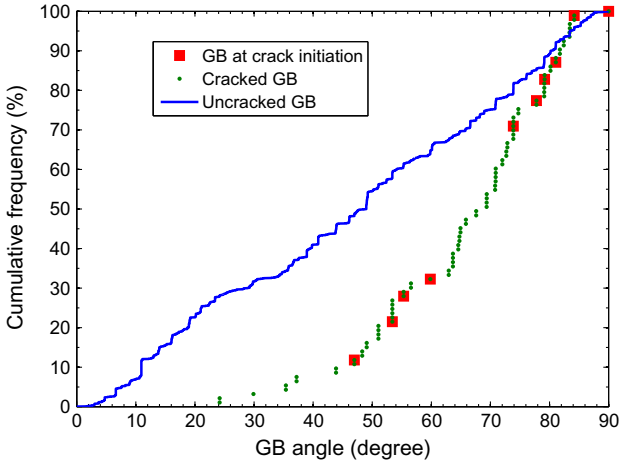

Fig. 11. Relative cumulative frequency of grain boundary orientation for grain boundaries at crack initiation (red squares), along the crack path (green dots) and in free of crack areas (blue line). (For interpretation of the references to colour in this figure legend, the reader is referred to the web version of this article.)

Without mechanical stress, the weld nugget is sensitive to pitting corrosion without any intergranular attack. However, in the presence of a stress field at the local scale (due to an externally applied macroscopic stress or to internal residual stress) pitting corrosion is replaced by well developed intergranular stress corrosion cracking. Cracking morphology depends drastically on the mechanical field at the microstructural level. During low strain rate tests (uniaxial loading in the L direction at a strain rate of $10^{-6}\ s^{-1}$), crack propagation occurs along the T direction on the L–T surface of the specimens. Exposure of the 10% prestrained material to the corrosive environment leads to intergranular cracking having no preferential direction. In this condition, isotropic crack branching

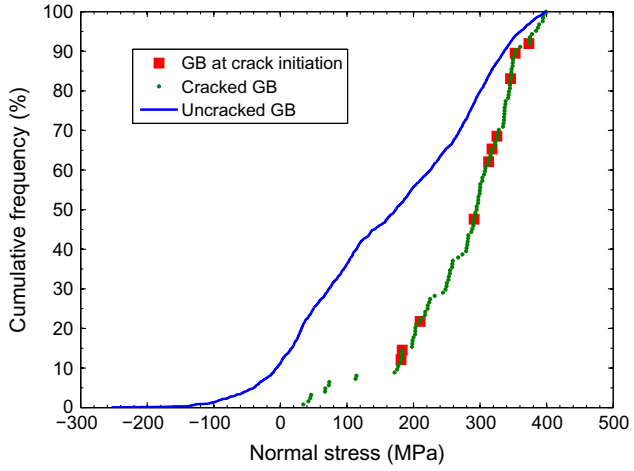

Fig. 12. Relative cumulative frequency of normal stress at grain boundary for grain boundaries at crack initiation (red squares), along the crack path (green dots) and in free of crack areas (blue line). (For interpretation of the references to colour in this figure legend, the reader is referred to the web version of this article.)

is observed after crack initiation. EBSD analysis of surface specimen after stress corrosion cracking tests has shown the crucial effect of textured bands induced by the welding process. The longest cracks initiate and propagate along the interface of the textured bands. From investigations at the local scale, it was demonstrated that the grain boundary character has no significant effect on crack initiation. The angle between the grain boundary and the direction of the macroscopic loading is a more relevant parameter. FE simulation using crystal plasticity on smooth aggregates built from EBSD maps of zones containing cracks, have confirmed that the key parameter is the normal stress. The normal stress threshold at grain boundary for stress corrosion cracking initiation is about 80% of the nominal macroscopic stress.

Acknowledgment

This work was financially supported by the ANR MatetPro program ANR-08-MAPR-0020-05 (Coralis project, Corrosion of aluminum Lithium Structures).

References

[1] G. Pouget, A. Reynolds, Int. J. Fatigue 30 (3) (2008) 463–472.
[2] V. Proton, J. Alexis, E. Andrieu, C. Blanc, J. Delfosse, L. Lacroix, G. Odemer, J. Electrochem. Soc. 158 (5) (2011) C139–C147.
[3] E. Bousquet, A. Poulon-Quintin, M. Puiggali, O. Devos, M. Touzet, Corros. Sci. 53 (9) (2011) 3026–3034.
[4] M. Jariyaboon, A.J. Davenport, R. Ambat, B.J. Connolly, S.W. Williams, D.A. Price, Corros. Sci. 49 (2007) 877–909.
[5] O. Hatamleh, P.M. Singh, H. Garmestani, Corros. Sci. 51 (1) (2009) 135–143.
[6] R. Fonda, P. Pao, H. Jones, C. Feng, B. Connolly, A. Davenport, Mater. Sci. Eng. A 519 (2009) 1–8.
[7] R.G. Buchheit, J.P. Moran, G.E. Stoner, Corrosion 50 (2) (1994) 120–130.
[8] R.G. Buchheit Jr., J.P. Moran, G.E. Stoner, Corrosion 46 (8) (1990) 610–617.
[9] C. Kumai, J. Kusinski, G. Thomas, T.M. Devine, Corrosion 45 (4) (1989) 294–302.
[10] J. Li, C. Li, Z. Peng, W. Chen, Z. Zheng, J. Alloys Compd. 460 (1–2) (2008) 688–693.
[11] S. Kim, U. Erb, K. Aust, G. Palumbo, Scripta Mater. 44 (5) (2001) 835–839.
[12] L. Chan, H. Weiland, S. Cheong, O. Rohrer, A. Rollett, in: A.D. Rollett (Ed.), Applications of Texture Analysis, John Wiley & Sons, Inc., Hoboken, NJ, 2008, pp. 261–268.
[13] X. Liu, G. Frankel, B. Zoofan, S. Rokhlin, Corros. Sci. 46 (2) (2004) 405–425.
[14] X. Liu, G. Frankel, B. Zoofan, S. Rokhlin, Corros. Sci. 49 (1) (2007) 139–148.
[15] H. Vogt, M. Speidel, Corros. Sci. 40 (2-3) (1998) 251–270.
[16] P. Srinivasan, K. Arora, W. Dietzel, S. Pandey, M. Schaper, J. Alloys Compd. 492 (1–2) (2010) 631–637.
[17] P. Srinivasan, W. Dietzel, R. Zettler, J. dos Santos, V. Sivan, Mater. Sci. Eng. A 392 (1–2) (2005) 292–300.
[18] M. Touzet, F. Le Poulain, I. Aubert, M. Puiggali, Mech. Mater. 38 (7) (2006) 620–632.
[19] K.R. Cooper, R.G. Kelly, in: Topical Day on Numerical Simulation of Localised Corrosion, SCK-CEN, Belgium, 2002.
[20] K. Saito, J. Kuniya, Corros. Sci. 43 (9) (2001) 1751–1766.
[21] R. Fonda, J. Bingert, Scripta Mater. 57 (11) (2007) 1052–1055.
[22] G. Cailletaud, S. Forest, D. Jeulin, F. Feyel, I. Galliet, V. Mounoury, S. Quilici, Comput. Mater. Sci. 27 (3) (2003) 351–374.
[23] V. Proton, J. Alexis, E. Andrieu, J. Delfosse, M.-C. Lafont, C. Blanc, Corros. Sci. 73 (2013) 130–142.